nature

SUPPLEMENTARY INFORMATION

https://doi.org/10.1038/s41586-019-1022-9

In the format provided by the authors and unedited.

Particle robotics based on statistical mechanics of loosely coupled components

Shuguang Li[1,2,6]*, Richa Batra[2,6]*, David Brown[3], Hyun-Dong Chang[3], Nikhil Ranganathan[3], Chuck Hoberman[4,5], Daniela Rus[1] & Hod Lipson[2]*

[1]Computer Science and Artificial Intelligence Laboratory, Massachusetts Institute of Technology, Cambridge, MA, USA. [2]Creative Machines Laboratory, Mechanical Engineering Department, Columbia University, New York, NY, USA. [3]School of Mechanical and Aerospace Engineering, Cornell University, Ithaca, NY, USA. [4]Graduate School of Design, Harvard University, Cambridge, MA, USA. [5]Wyss Institute for Biologically Inspired Engineering, Harvard University, Cambridge, MA, USA. [6]These authors contributed equally: Shuguang Li, Richa Batra. *e-mail: lisg@csail.mit.edu; richa.batra@columbia.edu; hod.lipson@columbia.edu

Supplementary Information

Particle robotics based on statistical mechanics of loosely-coupled components

Shuguang Li,[1,2]* Richa Batra,[2]* David Brown,[3] Hyun-Dong Chang,[3] Nikhil Ranganathan,[3]
Chuck Hoberman,[4,5] Daniela Rus,[1] Hod Lipson[2]

Contents:

[1]Computer Science and Artificial Intelligence Laboratory, Massachusetts Institute of Technology, Cambridge, MA 02139, USA.
[2]Creative Machines Laboratory, Mechanical Engineering Department, Columbia University, New York, NY 10027, USA.
[3]School of Mechanical and Aerospace Engineering, Cornell University, Ithaca, NY 14850, USA.
[4]Graduate School of Design, Harvard University, Cambridge, MA 02138, USA.
[5]Wyss Institute for Biologically Inspired Engineering, Harvard University, Cambridge, MA 02138, USA.
*These authors contributed equally to this work

S1. Particle Design

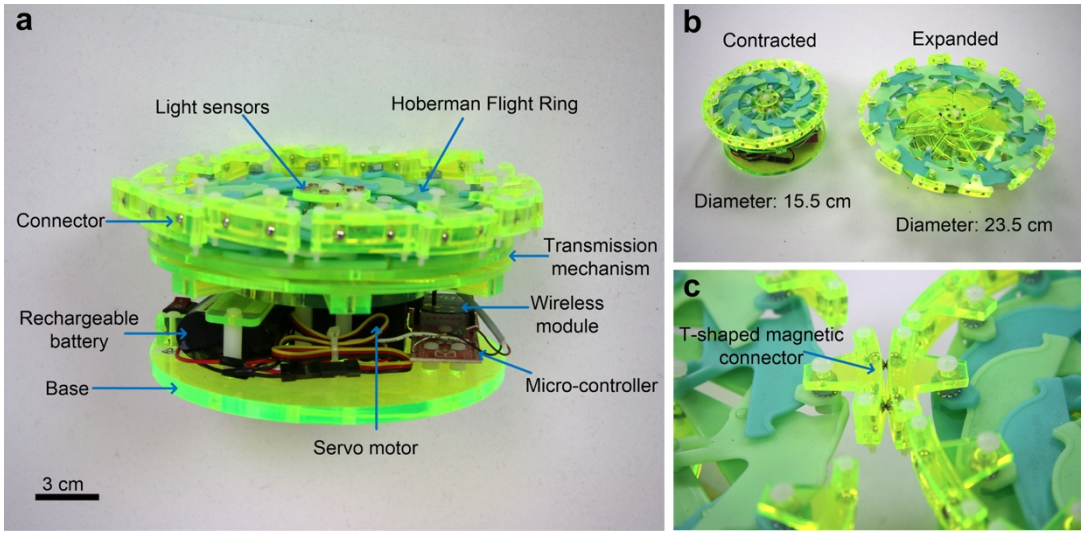

Figure S1: (a) A single particle structure, (b) particles in expanded and contracted states, and (c) a close-up view of magnetic connectors.

The structural parts—the base plate, guiding plates, rotating disc, and T-shaped connectors—were cut from green acrylic sheets using laser beam. Nylon screws were used as the sliding pins to drive the Hoberman Flight Ring™, as well as the pivots for the connectors on the outer perimeter. To accommodate the pins and pivots, small holes were drilled on both the inner and the outer Flight Ring perimeter. A set of nylon standoffs and metal screws was used to support the upper half of the structure, leaving enough space for the electronic parts, which are listed in Table S1.

A circular, 6 mm-thick acrylic plate served as the particle base, as it offers a smooth bottom surface, allowing the particle to slide on the ground. It also supports the particle's structure and functional parts, including the servo, micro-controller, wireless communication module, rechargeable battery, and power switch. In addition, an array of six Cadmium Sulfoselenide (CdS) photoelectric sensors were mounted on the top in the center to measure the intensity of environmental light. A Hoberman Flight Ring™ was modified to produce the required radial expansion and contraction (Fig. S1a).

Table S1: Parts list of the particle

Item	Model	Manufacturer	Details
Microcontroller	Arduino Fio v3	SparkFun Electronics	ATmega32U4 running at 8MHz
Photo sensors	PDV-P9006	Advanced Photonix Inc	CdS Photoconductive photocells (×6)
Wireless module	XBee S1	Digi International Inc.	XBee 1mW wire antenna - Series 1 (802.15.4)
Rechargeable battery	31004	Tenergy Corporation	Li-Ion 7.4V 2600mAh rechargeable battery pack
Servo	HS-430BH	Hitec RCD USA, Inc	Maximum torque range: 5.0 kg.cm
Load	RNV14FAL1M50 CT-ND	Stackpole electronics Inc.	1.5 MΩ, high voltage anti-moisture metal film resistor
Battery charger	TLP-2000	Tenergy Corporation	Li-Ion/Li-Po battery pack charger: 3.7V-14.8V

Particle expansion and contraction was driven by the servo motor and transmission mechanism, which consisted of a rotating disc with curved slots, an upper and lower guiding plate, and seven sliding pins fixed to the Flight Ring (Fig. S2). The rotating disc was directly connected to the servo motor shaft. During rotation, constrained by the curved slots of the rotating disk and the radial slots of the guiding plates, the pins fixed to the Flight Ring slide outward and inward from the particle center, thereby expanding and contracting the Flight Ring in congruity.

Each particle can expand and contract in a continuous manner, resulting in variable diameter ranging from 15.5 cm to 23.5 cm (Fig. S1b). In addition, 14 T-shaped connectors with the ability to passively pivot were arranged at equal angular intervals along the outer perimeter of the top disc. Two 5 mm-diameter spherical neodymium magnets were enclosed inside each connector with sufficient space to freely rotate. Through small outward-facing openings, the magnets included in one particle can directly connect with those attached to other particles (Fig. S1c). These magnetic forces create adhesion between adjacent particles, resulting in densely-packed configurations. The design flexibility also allows for adjacent particles to maintain contact while they expand and contract at different rates.

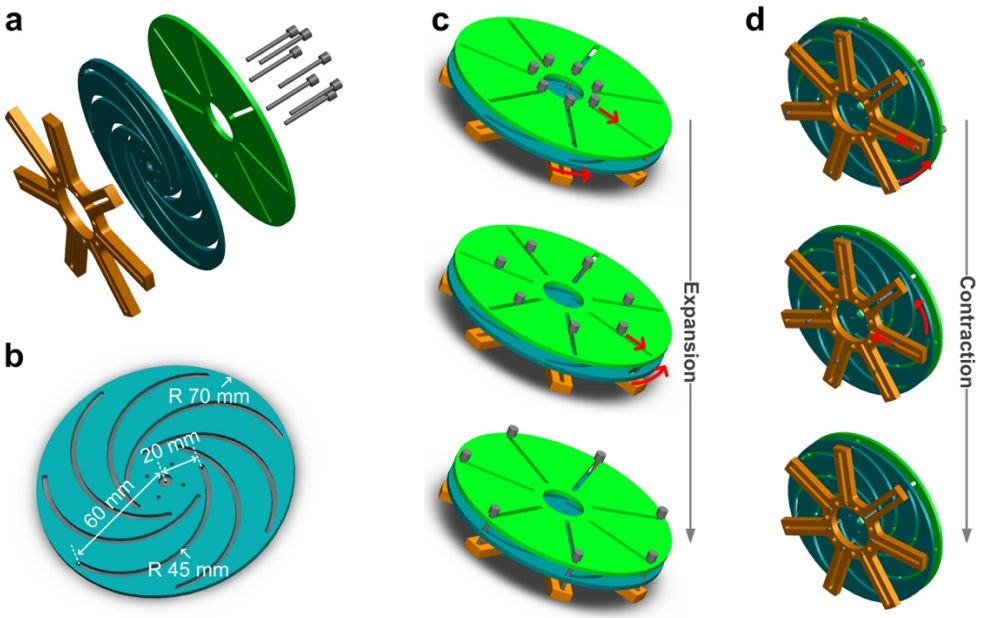

Figure S2: Particle transmission mechanism. (a) Transmission parts and structure. (b) Rotational disc dimensions. (c) Expansion process and (d) contraction process.

S2. Particle Robot Locomotion

As the particles expand and contract radially, their center of gravity does not move during this cyclical motion. Thus, to achieve a single-step sliding motion on the ground, the particle needs a larger, fixed object to collide with, including the surrounding static particles. In other words, a particle must produce an outward force during expansion that is greater that the static friction between its bottom layer and the ground, but is less than the friction experienced by the other particles, thereby causing it to slide away from the other members of the aggregate. Furthermore, the magnetic forces must exceed the static friction experienced by the particle, but remain below the overall static friction of the group, to ensure that the contracting particle will slide towards the other particles and maintain the connection. These force requirements for a single particle can be written as:

$$m \times g \times \mu_{static} < F_{expansion} < n \times m \times g \times \mu_{static} \quad (1)$$

$$m \times g \times \mu_{static} < F_{contraction} < n \times m \times g \times \mu_{static} \quad (2)$$

where n is the number of the particles acting as the static object and m is the mass of a single particle.

For a group of connected particles, locomotion can be achieved if their expansion and contraction is coordinated (Fig. S3). Specifically, as expansion of one particle propels its center of gravity outward, as it contracts, the subsequent particle expands, allowing it to maintain its new position. The center of gravity of the subsequent particle has also moved outwards in the same direction. This motion propagates until the final particle is reached, which also slides in that direction during its contraction. As a result of this chain of motion, the group moves forward or backward by ΔS distance, once all the particles have finished their single-step sliding motions. The actuation sequence of individual particles determines the sliding direction of the group, whereby the particles produce an expansion−contraction "wave" that propagates in the opposite direction of their locomotion.

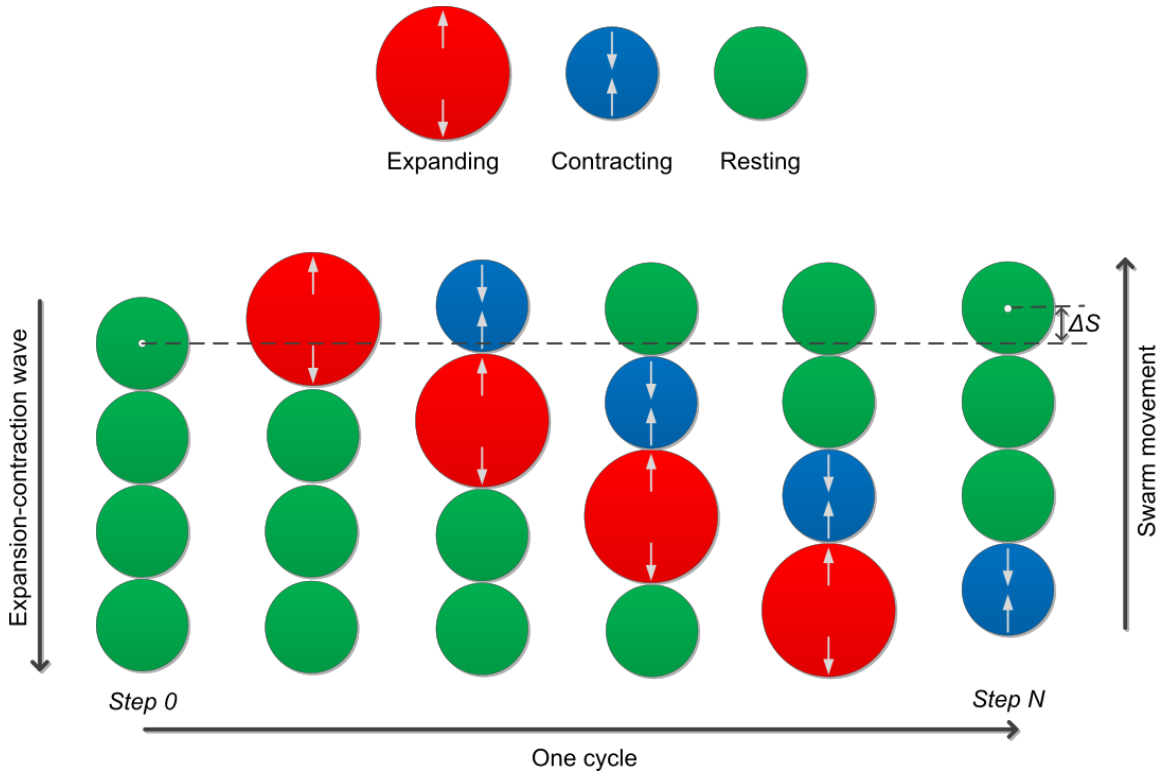

Figure S3: Illustration of particle robot locomotion. Particles expand and contract sequentially to generate a net forward locomotion.

In order to achieve a continuous movement, each particle in the group needs to periodically run a full expansion−contraction cycle, with a pause (resting time) between cycles. This pause is set to a constant time interval, in order to allow other particles in the group to complete their sliding motion without canceling the net movement of the group. Thus, the duration of this pause t_p is determined by the minimum number of particles per wave (N) for an efficient single-step sliding, which was set as

$$t_p \geq (N-1)\times\frac{1}{2}T \tag{3}$$

In this study, the expansion and contraction of individual particles was set to follow a sinusoid function:

$$R(t) = \frac{\Delta R}{2}\times\left(1+\sin\left(2\pi f t - \frac{\pi}{2}\right)\right) + R_{min} \tag{4}$$

where *R(t)* represents the particle radius at moment *t*, R_{min} is its minimum radius (fully contracted), ΔR denotes the maximum expanded radius of the particle (fully expanded), *f* is the expansion−contraction frequency, and *t* is the relative time within a cycle. Moreover, the delay between the sequential actuation is set to $\frac{1}{2}T$, ensuring that each particle starts to run at t_I (global time):

$$t_I = (S_n - 1) \times \frac{1}{2} T \tag{5}$$

where S_n is the actuation, or phase delay, sequence index of the particle in the group, and *T* is the period of each expansion−contraction cycle.

S3. Sensor Characterization

CdS photocells are widely used for detecting environmental light, since their resistances can vary depending on different light intensity levels. In the context of the present study, light intensity is defined as the light illuminance level at the individual particle's radial position (distance) from the light source. It is further assumed that the light intensity decays with the increase of radial distance following the inverse-square law, yielding the following expression:

$$I_n = \frac{L_s}{4\pi r_n^2} = \frac{I_s}{r_n^2} \tag{6}$$

where L_s and I_s are the light source's luminous flux and luminous intensity, respectively, and r_n is the particle's radial distance from the light source. In the present investigation, the luminous flux and intensity of the light source were maintained at the constant level in all experiments.

The sensitivity performance of a CdS photocell can be characterized by γ, defined as

$$\gamma = \frac{\log R_{100} - \log R_{10}}{\log I_{10} - \log I_{100}} \tag{7}$$

where R_{100} and R_{10} are the resistances at 100 (I_{100}) lux and 10 (I_{10}) lux, respectively. The γ value of the sensors employed in the present work is ≈1.0. This relationship can be used to estimate a particle's position in dark room environment based on the measured light intensity. From Equation (7), the following equalities can be derived:

$$\gamma = \frac{\log R_n - \log R_x}{\log I_x - \log I_n} = \frac{\log \frac{R_n}{R_x}}{\log \frac{I_x}{I_n}} = 1 \tag{8}$$

$$\frac{R_n}{R_x} = \frac{I_x}{I_n} \tag{9}$$

where R_n and R_x are the resistances at different positions corresponding to the measured light intensities of I_n and I_x. Introducing the light intensity definition into Equation (9) allows the relationship between the photocells' resistances and the particles' positions to be expressed as:

$$R_n = \frac{I_x}{I_n} R_x = \left(\frac{r_n}{r_x}\right)^2 R_x \tag{10}$$

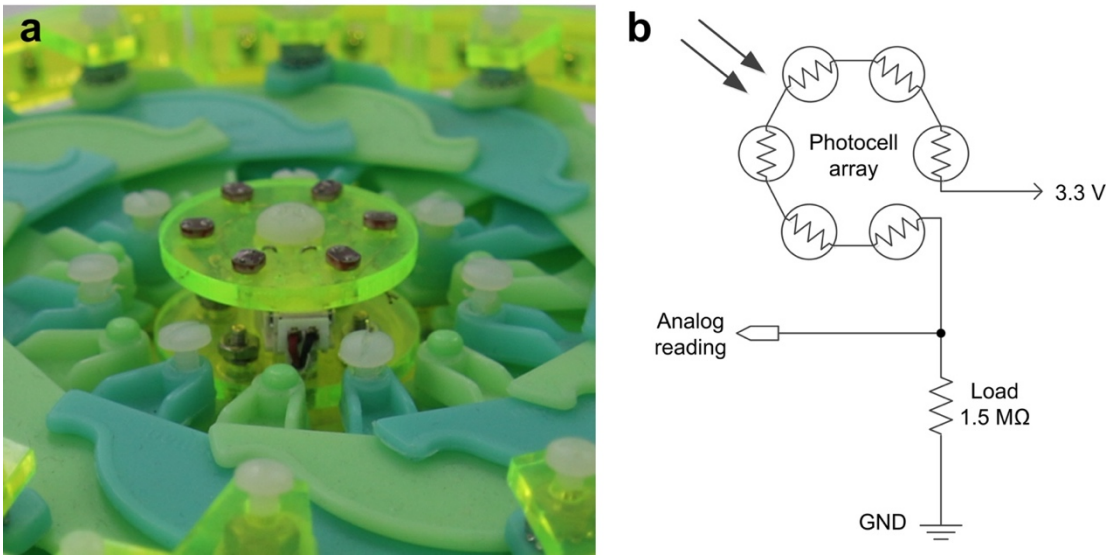

Figure S4: Characterization of the light intensity sensors. (a) Sensor array and (b) measurement circuit.

To obtain the light intensity pseudo-value, the analog values of load resistor voltages can be measured through the on-board voltage-divider circuits (Fig. S4) and subsequently converted to their digital equivalents (0~1023). As previously noted, the light intensity value V_n decreases as the particle's distance r_n increases and vice versa. The digital equivalents of the load's analog voltage values can also be calculated by:

$$V_n = 1023 \times \frac{R_R}{R_n + R_R} = 1023 \times \frac{R_R}{\left(\frac{r_n}{r_x}\right)^2 R_x + R_R} \tag{11}$$

$$V_x = 1023 \times \frac{R_R}{R_x + R_R} \tag{12}$$

$$R_x = \frac{(1023 - V_x)R_R}{V_x} \tag{13}$$

where R_R denotes the 1.5 MΩ load resistance. From these equations, the particle positons can be estimated using the following relationship:

$$r_n{}^2 = \frac{V_x(1023 - V_n)}{V_n(1023 - V_x)} r_x{}^2 \tag{14}$$

As indicated by Equation (14), for estimating a particle's position r_n, it is necessary to obtain its intensity measurement (voltage) V_n, as well as determine the reference particle's position r_x and light intensity V_x.

To characterize and verify the sensor system performance, measurements were conducted using an array of nine particles arranged in a straight line, starting from the light source's projection center. In this experiment, the particle below the lamp was chosen as the reference particle (see Fig. S5a), with $r_1 \approx 28$ cm and V_1 measured at 980. The particles' planar positions (linear distances) D_n along the straight line on the ground can be calculated by

$$D_n = \sqrt{r_n{}^2 - r_x{}^2} \tag{15}$$

The true positions and the estimated positions of the particles are shown in Fig. S5b, where each estimation represents an average based on five trials. This result indicates that the particles' relative positions can be successfully estimated using the light intensity measurements. Similarly, the light intensity levels can also be predicted in this experiment, if the true positions of the particles are known. The error bars represent one standard deviation from the mean.

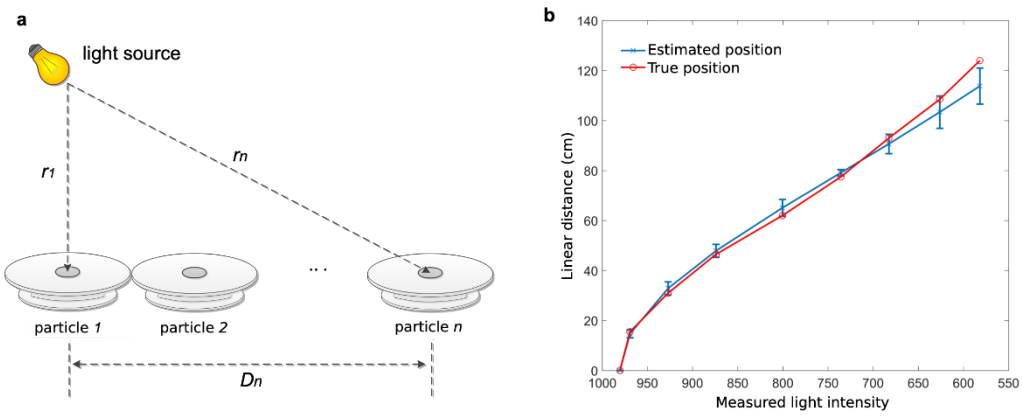

Figure S5. Light intensity measurement and position estimation. (a) Experimental setup and (b) test results.

As shown in Fig. S6a, all locomotion tests were conducted in a dark room, and a group of four lighting soft-boxes with 85 W bulbs (Neewer Technology Co., Ltd) were used for videos and photos when needed. The particles were placed on a flat and clean horizontal surface of 320 × 200 cm^2 area. In order to build the test ground, a polypropylene and latex rug of 5 mm thickness (Garland Sales, Inc.) was placed directly on the room floor, and was covered by a blackout cloth projector screen film of 0.35 mm thickness comprising of 70% polyester and 30% cotton with rubber coating (Carl's Place LLC). A high-definition webcam (C920 HD Pro, Logitech) situated 225 cm above the floor was used to record the experiments from top-view. This camera setup can capture a test field of approximately 285× 160 cm^2 area. The static "wall" and "obstacle" in our experiments were made of 38 cm tall cylindrical plastic shipping jugs of 29 cm diameter (McMaster-Carr Supply Company).

For the phototaxis experiments, 35 cm tall desktop lamps with 25 W yellow color incandescent bulbs (McMaster-Carr Supply Company) served as light sources. The particles and light bulb(s) were placed in random configurations by the experimenter (Fig. S6b). A voltage-divider circuit (1.5 MΩ load resistance) was used to provide an analog reading of the voltage over the load, which was subsequently converted to a digital value corresponding to the light intensity (1023~0). Each intensity reading is an averaged value based on 50 independent measurements. A USB-based Xbee module (XBee Explorer, SparkFun Electronics) and the X-CTU software (Digi International Inc.) were used to receive the particles' broadcasts and transmit global start/stop commands to the particles. The communication baud rate was set at 9600.

Figure S6: Locomotion Testing. (a) Experimental set-up for robot locomotion and (b) initial configurations of the nine locomotion experiments.

S4. Relative Position (Light Intensity) Estimation

Several methods can be used to determine the particle's position based on light intensity measurements, such as applying the inverse square relationship between light intensity and distance, or self-ranking based on broadcast readings. While different methods were employed in the locomotion experiments, no statistically significant differences in their effectiveness were noted.

A. Direct estimation without communication

One of the simplest methods for estimating a particle's relative position is based on the application of Equations (14) and (15) given above. Once a reference position and its light intensity are known—which can be chosen arbitrarily, corresponding to, for example, the location with the highest intensity in the field—each particle's position (relative to the reference position) can then be estimated based on its intensity measurement. In the tests conducted as a part of this work, the point directly below the light bulb was chosen as the reference position, at 28 cm vertical distance to the light source center. The light intensity of 980 was measured at this reference position. Therefore, each robot particle's planar distance D_n to the reference point could be calculated, and the actuation sequence index S_n could be obtained by applying the expression below:

$$S_n = \frac{D_n}{D} \tag{16}$$

where D is the minimal diameter of the particle, which was approximately 15.5 cm in all experiments, based on this particular particle design. This method offers a quick and accurate means of estimating each particle's relative position and intensity level within a group, based on the *a priori* determined values of the chosen reference point's position and the corresponding light intensity.

B. Communication based linear approximation method

The actuation sequence index or the signal intensity level can also be quickly approximated by applying a linear proportional method through particle−particle communication. Here, it is assumed that the light intensity decreases linearly as the planar distance between the particle and

the light source increases. Thus, the particles can then be equally divided into N_w groups separated by the intensity decrement of ΔV, which can be calculated from the expression below:

$$\Delta V = \frac{V_{max} - V_{min}}{N_w} \tag{17}$$

Using this value, the particle's actuation sequence index or intensity level S_n can be calculated via:

$$S_n = \frac{V_{max} - V_n}{\Delta V} \tag{18}$$

While the communication-based method provides a quick estimate, its accuracy is relatively low due to the assumption of the existence of a linear relationship between the light intensity and distance.

C. Nonlinear distance−intensity relationship-based method

If the light source and a group of particles are assumed to be located in a planar field, then the relative position (signal intensity level) of a particle can be estimated from the communications among the particles. The height difference between the sensors and the light source is ignored in this case. As shown in Fig. S7, the reference point *x* was chosen, whereby its radial distance to the center of the light source is *xD*, where D represents the diameter of a particle when contracted. The distance of the nearest (leader) particle to the light source is defined as *KD*. As the body length of the robot group comprising of *N* particles is *ND* in the radial direction, distance between the farthest particle and the light source is *(K+N)D*. Similarly, an arbitrary particle's radial distance to the light source can be expressed as *(K+n)D*, where n is the particle's relative position (intensity level) within the group. The light intensities of the reference point, the nearest particle, the farthest particle, and a particle in the group are denoted as I_x, I_{max}, I_{min}, and I_n, respectively. As shown in Equations (19)−(29) given below, the ratios between those distances are denoted by *a, b, c,* and ρ. Therefore, each of the particles' relative positions (intensity level) S_n can be estimated by applying Equation (30) based on its own intensity level, the maximum intensity, and the minimum intensity of the group. This method yields a very accurate estimation of the relative position (light intensity level) for each particle in a 2D field.

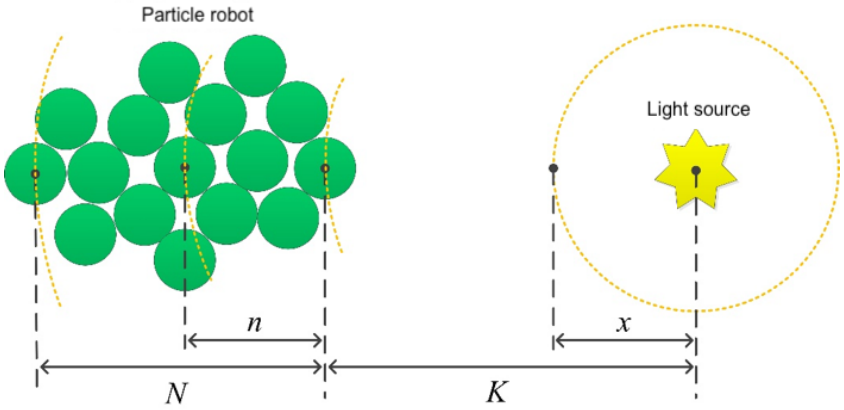

Figure S7: Distance−intensity relationship-based estimation illustration.

$$I_n = \frac{L_s}{4\pi r_n^2} = \frac{I_s}{r_n^2} = \frac{I_s}{(K+n)^2 D^2} \tag{19}$$

$$I_x = \frac{I_s}{x^2 D^2} \tag{20}$$

$$I_{max} = \frac{I_s}{K^2 D^2} \tag{21}$$

$$I_{min} = \frac{I_s}{(K+N)^2 D^2} \tag{22}$$

$$\frac{I_x}{I_{max}} = \left(\frac{K}{x}\right)^2 = \frac{R_{max}}{R_x} \tag{23}$$

$$\frac{I_x}{I_{min}} = \left(\frac{K+N}{x}\right)^2 = \frac{R_{min}}{R_x} \tag{24}$$

$$\frac{I_x}{I_n} = \left(\frac{K+n}{x}\right)^2 = \frac{R_n}{R_x} \tag{25}$$

$$a = \frac{K}{x} = \left(\frac{R_{max}}{R_x}\right)^{\frac{1}{2}} \tag{26}$$

$$b = \frac{K+N}{x} = \left(\frac{R_{min}}{R_x}\right)^{\frac{1}{2}} \tag{27}$$

$$c = \frac{K+n}{x} = \left(\frac{R_n}{R_x}\right)^{\frac{1}{2}} \tag{28}$$

$$\rho = \frac{n}{N} = \frac{c-a}{b-a} = \frac{(R_n)^{\frac{1}{2}} - (R_{max})^{\frac{1}{2}}}{(R_{min})^{\frac{1}{2}} - (R_{max})^{\frac{1}{2}}} = \frac{\left(\frac{1023-V_n}{V_n}\right)^{\frac{1}{2}} - \left(\frac{1023-V_{max}}{V_{max}}\right)^{\frac{1}{2}}}{\left(\frac{1023-V_{min}}{V_{min}}\right)^{\frac{1}{2}} - \left(\frac{1023-V_{max}}{V_{max}}\right)^{\frac{1}{2}}} \tag{29}$$

$$S_n = N_w \times \rho \tag{30}$$

D. Stronger intensity level counting method

The particle's intensity level can also be estimated by conducting pairwise comparisons of the intensity levels among the particles within the group through particle−particle communication. In this estimation process, each particle broadcasts its own light intensity level to the group, as well as receives the intensity levels from other particles. The received information is then compared with the particle's own intensity level and the record of stronger intensity levels. A received intensity level is counted as a new stronger intensity level only when it is stronger than the particle's own intensity, and it is distinct from any of the previously recorded stronger intensities. Finally, a count of stronger intensity-level is obtained for each particle after this process, which can be directly used as the relative position and intensity level S_n. The steps pertaining to this method are given in Algorithm 4. In the experiments performed as a part of this investigation, the distinguishable intensity difference was defined as ±10 for the intensity-level comparison, and each particle's intensity measurement was broadcast repeatedly five times during each estimation process. Although this method is simple and efficient, a record of "stronger intensity" is needed for each particle.

S5. Control Algorithms for Particle Robot Phototaxis

Algorithm 1: Light intensity/gradient measurement and relative position estimation

For each particle

Measure its light intensity

Broadcast the measured light intensity

Receive the relevant light intensity measurements from the group (i.e., the Max or Min values)

Estimate its relative position to the light source from the known light intensity values

Obtain its actuation sequence index S_n based on the estimated position

End

Algorithm 2: Coordinated locomotion

For each particle

Get the actuation sequence index S_n and actuation period T

Set the local time $t = 0$

Wait for an initial time t_I

Repeat

    Run expansion−contraction cycle with the period T

    Pause for a resting time t_p

Until $t >$ update time

End

Algorithm 3: Automatic phototaxis motion

For each particle

Repeat

    Light intensity/gradient measurement and relative position estimation

    Coordinated locomotion

Until the measured light intensity does not increase anymore

End

Algorithm 4: Stronger intensity-level counting

For each particle

1 **Initialize** the stronger intensity counter and record, *SI_Number* ← *0* and *SI_Record* ← *empty*

2 **Get** its current light intensity I_n

3 **Repeat**

4 **Receive** intensity information I_o from other particles via communication (broadcast messages)

5 **If** I_o is not null and $I_o > I_n$

6 **If** I_o is not equal (close) to any of the previous intensity records from *SI_Record* **then**

7 **Save** I_o into the stronger intensity record (array), *SI_Record* ← I_o

8 **Update** the stronger intensity level counter, *SI_ Number* ← *SI_ Number +1*

9 **End if**

10 **End if**

11 **Until** broadcasts end

12 **Return** *SI_ Number*

13 **End**

S6. Statistical Analysis of Experiments

The video recordings of the phototaxis experiments were processed in Matlab to track the particle robot centroid over time. The processing commenced by converting the frames to grayscale and enhancing the contrast, followed by edge detection, binarization, suppressing the light source, morphological operations, and finally perimeter tracing of the agglomerate particles. The extracted perimeter was subsequently used to infer the particle robot centroid. Fig. S8 shows typical intermediate results of the aforementioned sequence of processes for analyzing a single frame.

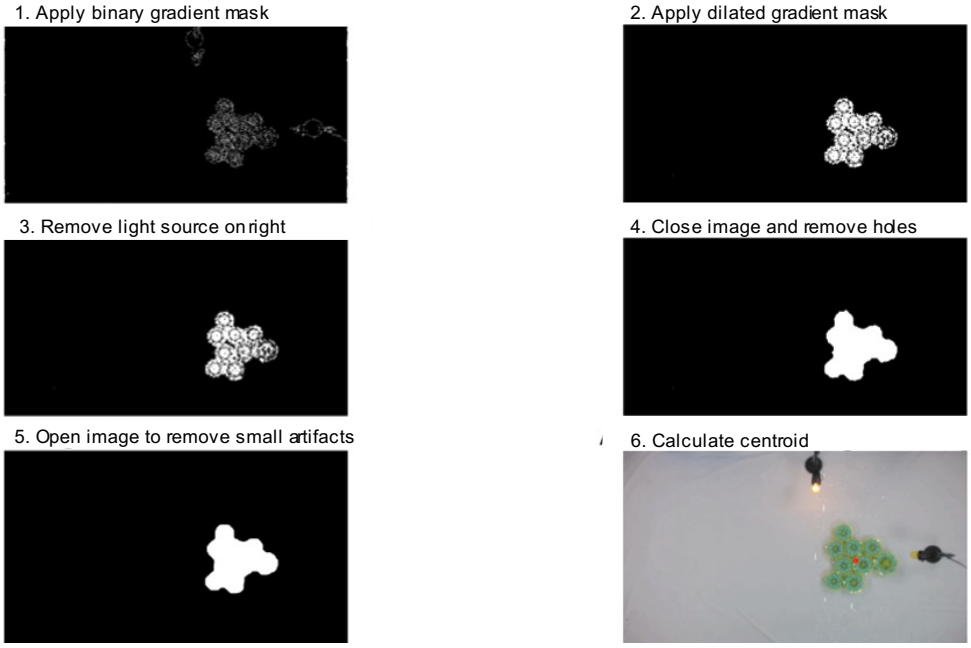

Figure S8: Analysis of phototaxis experiments. The steps used to process the experiment recordings are shown with an example video frame. The final step shows the original image with the centroid superimposed.

To facilitate automated video processing, the particle robot was approximated as a continuous and uniform region when determining the centroid, as opposed to tracing the position of each particle and treating the particles as point masses to calculate the robot centroid. This approximation, however, introduces noise to the centroid data by being biased towards the expanding particles in any given frame. To mitigate this issue, subsequent statistical analysis on centroid locations inferred at 30 s intervals was performed, corresponding to approximately 3.5

expansion−contraction cycles. As a part of this analysis, the frame of reference was transformed to ensure that the initial centroid defines the coordinate system origin and the stimulus defines a point on the positive y-axis. Within this frame of reference, one-tailed t-tests were conducted for the motion in the y-direction, whereby the null hypothesis postulated that the motion in the y-direction is random with a mean of zero. In each experiment, the null hypothesis was rejected with $p < 0.01$, indicating statistically significant locomotion towards the light source. These results are shown in Table S2.

Table S2: Statistical results of phototaxis experiments. One-tailed t-tests were performed on the motion results of nine locomotion experiments. The average speed and peak speeds are also included. The ordering of the images in the table corresponds to Fig. 3d and Fig. S6b.

Number	Control Method	Average Speed (% min. diameter/cycle)	Peak Speed (% min. diameter/cycle)	P-Value
1	(A) Direct estimation without communication	3.03	8.96	3.1309e-07
2	(A) Direct estimation without communication	1.90	6.74	3.1668e-09
3	(A) Direct estimation without communication	2.61	7.99	1.0892e-07
4	(C) Nonlinear distance-intensity relationship method	1.79	5.02	3.5582e-07
5	(D) Stronger intensity counting method	3.13	12.89	6.7304e-09
6	(C) Nonlinear distance-intensity relationship method	1.95	6.14	3.3364e-04
7	(C) Nonlinear distance-intensity relationship method	3.10	12.13	3.3641e-04
8	(B) Communication based linear approximation method	2.05	5.11	1.2635e-05
9	(A) Direct estimation without communication	2.25	8.28	8.2513e-10

S7. Characterization of Forces Acting on Individual Particles

For the force measurements, a universal testing machine (Instron 5944, Instron Corporation) was used to characterize the adhesive force between the connectors, the pulling and pushing forces generated by the particle, and the friction between the particle and the test surface materials. For the adhesive force measurement, the Instron machine was controlled to pull apart two joined magnetic connectors at a speed of 0.1 mm/s (Fig. S9a). The applied forces and the connectors' separating distances were recorded, as shown in Fig. S9b. The peak adhesive force exerted by the connectors was approximately 4.5 N, based on five trials. The solid line in Fig. S9b represents the averaged values, while the shadow area represents the standard deviations.

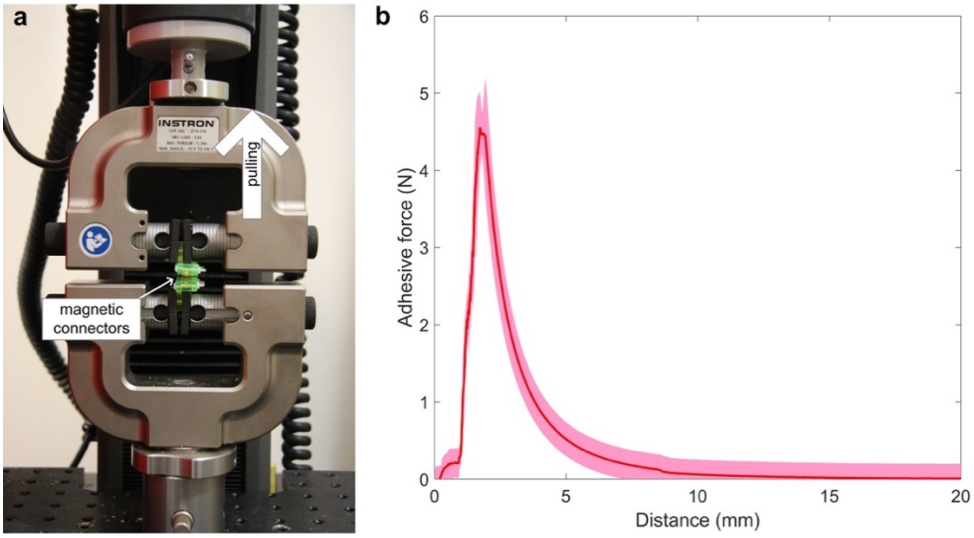

Figure S9: Measurements of particle-to-particle connection force. (a) Experimental setup and (b) test results.

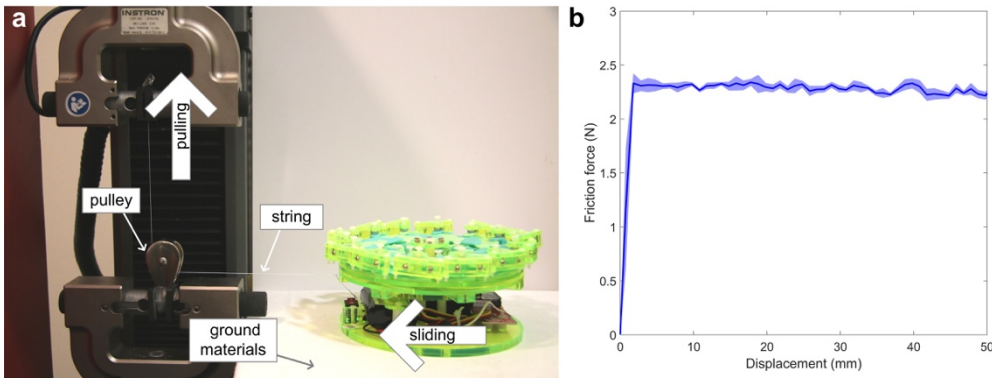

Figure S10: Measurements of friction between the particle and surface. (a) Experimental setup and (b) friction results.

To characterize the friction between the particle and the test surface, a flat platform (of 30×30 cm^2 area) covered by the same materials as those used in the experiments, was created. As shown in Fig. S10a, a particle was placed on this platform, and it was connected to the Instron machine through a thin string over a miniature metal pulley. The Instron machine was used to pull the particle, forcing it to slide across the platform at a constant speed (10 mm/s). The displacement and the pulling force were both recorded during the sliding. Fig. S10b shows that the maximum friction between the particle and the test surface was approximately 2.3 N, averaged across five trials. The solid line represents the average values, with the shadow area depicting the standard deviations.

To measure the pulling force, the particle was fixed vertically, and its one connector was linked to the Instron machine's upper gripper via a thin and inextensible string, as shown in Fig. S11a. In this test, the particle was programmed to contract from the maximum diameter to the minimum diameter. The Instron machine was controlled to follow the particle's contraction and rapidly balance the pulling force. For the pushing force measurements, the particle was programmed to extend radially from the minimum diameter to the maximum diameter. As shown in Fig. S11c, a separated connector was clamped on the Instron machine to ensure that the contact with the particle's connector is maintained during expansion. The Instron machine was set to freely move following the particle's expansion, while the required balance force was recorded. The results are shown in Fig. S11b and Fig. S11d. The maximum pulling force produced by the particle was approximately 9 N, whereas the maximum pushing force was approximately 8 N. Throughout the contraction process, the pulling forces typically exceeded 3 N, while the pushing forces were typically greater than 2 N throughout the expansion process.

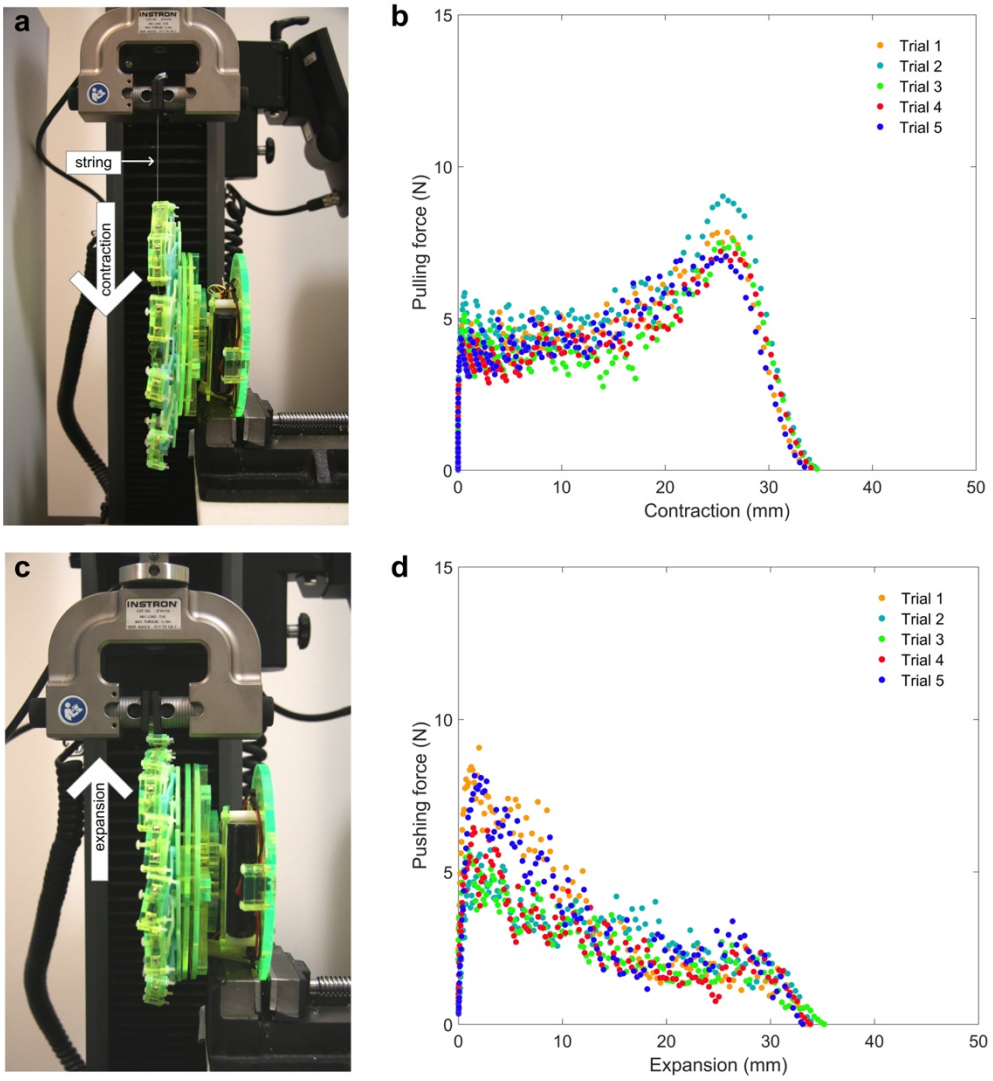

Figure S11: Measurements of the particle's pulling and pushing force. (a) Experimental setup for pulling force tests and (b) pulling force results. (c) Experimental setup for pushing force tests and (d) pushing force results.

To characterize the particle's contraction and expansion behavior, single expansion−contraction movement tests were conducted at different periodic lengths (speeds). Using a constant time for each step (20 ms), a particle was programmed to run the 75-step, 150-step, and 300-step expansion−contraction tests, respectively. Particle movements were recorded using a camera at 60 frames per second, and the particle's radius changes and time were both obtained using an open source image analyzing software (Tracker, http://physlets.org/tracker/). As shown in Fig. S12, the particle was able to expand and contract by approximately 35 mm in all three tests, and all the movement trajectories exhibit clear sinusoidal shapes, corresponding to the

controller design. The solid lines represent the results averaged over five trials for each test, and the shadow areas denote the corresponding standard deviations.

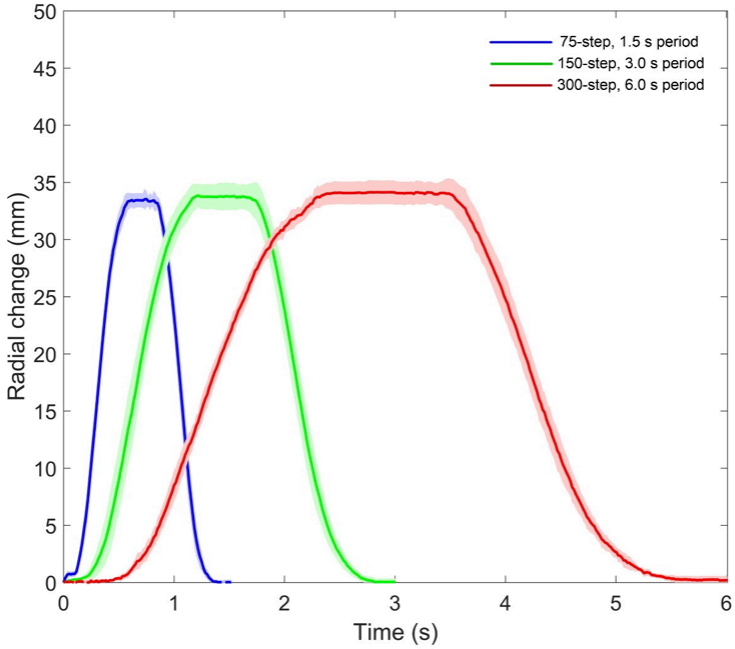

Figure S12. Particle expansion-contraction at different speeds. Radial change over time when motor steps are varied.

S8. Simulation Algorithm and Performance

The initial placement of the particles is determined through a randomized algorithm, detailed below. In general, the first three particles are placed adjacent to one another, and the remaining particles are positioned tangentially to at least one particle, without intersecting any placed particles. Fig. S13 shows random initial configurations of ten particles. This algorithm differs slightly from the experimental method, in which each particle is placed tangentially to at least two particles. At small scales this difference is negligible, i.e. particles with one adjacent neighbor attach to a second particle after one or two expansion-contraction cycles. At larger scales, with 1,000 or 10,000 particles, this algorithm results in more sparse configurations that don't reconfigure as quickly into dense formations. However, changing to algorithm to match the experimental method, such that each additional particle is placed tangent to at least two particles, is computationally taxing. To remedy this initial difference in particle density, the simulations were run for at least 2 hours, and the first 30 minutes were ignored when calculating speed.

Algorithm 5: Placement of particles in simulation

1 **Set** the first particle's position $p_1 \leftarrow (0,0)$
2 **Set** the second particle's position p_2 tangent to p_1, in a random normal direction θ
3 **Set** the third particle's position p_3 tangent to both p_1 and p_2, randomly selected
4 **Set** $placed \leftarrow 0$
5 **For** particle $i = 4{:}\,N$
6 **While** $placed = 0$
7 Randomly select placed particle from 1 to $i - 1$
8 Randomly select direction θ
9 **For** $increment = 0{:}\,2\pi$
Set $\theta_i \leftarrow \theta + increment$
10 **Set** p_i adjacent to selected placed particle at θ_i
11 **If** p_i does not intersect with any placed particles
14 **Set** $\theta \leftarrow 2\pi$ and $placed = 1$
15 **End if**
16 **End for**
17 **End while**
18 **End for**

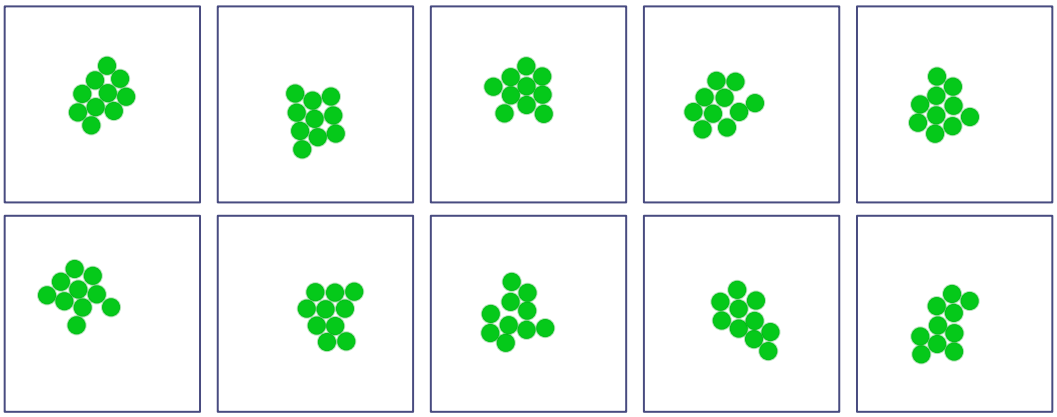

Figure S13: Initial configurations generated by simulation. Particles were generated by the particle robotics simulation for the dead-particle study in random initial configurations. The initial configurations of the ten-particle robots are shown in this illustration.

The simulation environment models the particle robotic algorithm and the physical particles using the experimental results. The variables are represented in the same notation as before, with T denoting the expansion−contraction time and t_p representing the pause duration. Given that the particles' phase delay is updated at 2−5 minute intervals during the experiments, to accurately replicate the experimental process, a variable N is introduced to represent the number of expansion−contraction cycles that the robot undergoes between phase updates. The simulation algorithm steps are presented below, and the code is available at the link shared in the main text.

Algorithm 6: Particle robot simulation

---

1 **Initialize** $t \leftarrow 0$, $n \leftarrow 0$, and particle positions p_i

2 **Set** particle radius $R_i \leftarrow R_{min}$, phase $\phi_i \leftarrow 0$, velocity $v_i \leftarrow 0$, repulsive forces $F_i^r \leftarrow 0$, and attraction force $F_i^a \leftarrow 0$ for each particle i

3 **If** $\left(t \geq T + t_p\right)$

4 **Set** $t \leftarrow 0$ and $n \leftarrow n + 1$

5 **End if**

6 **If** $(n \geq N)$

7 **Set** $n \leftarrow 0$

8 **Update** phase ϕ_i for each particle

9 **End if**

10 **For** each particle i

11 **If** $(\phi_i < t < T + \phi_i)$

12 **Update** R_i

13 **End if**

14 **For** each neighboring particle j

15 **Calculate** distance d_{ij}

16 **If** $d_{ij} < 0$

17 **Update** repulsive force F_i^r

18 **Else**

19 **Update** attraction force F_i^a

20 **End if**

21 **End for**

22 **For** each particle i

23 **Update** velocity v_i and position p_i

24 **End for**

25 **Increment** cycle time $t \leftarrow t + \Delta t$

26 **Repeat**

The simulation was validated against physical experiments. Fig. S14 shows the results of fitting the simulation of a robot comprised of five particles in a row to the corresponding experimental data. Fig. S15 shows comparative results obtained from simulation verification, based on a ten-particle robot in an amorphous configuration using the same parameters. Additionally, Fig. S16 compares the directional variability between the nine experiments to the simulation results, varying from ten particles to ten thousand particles.

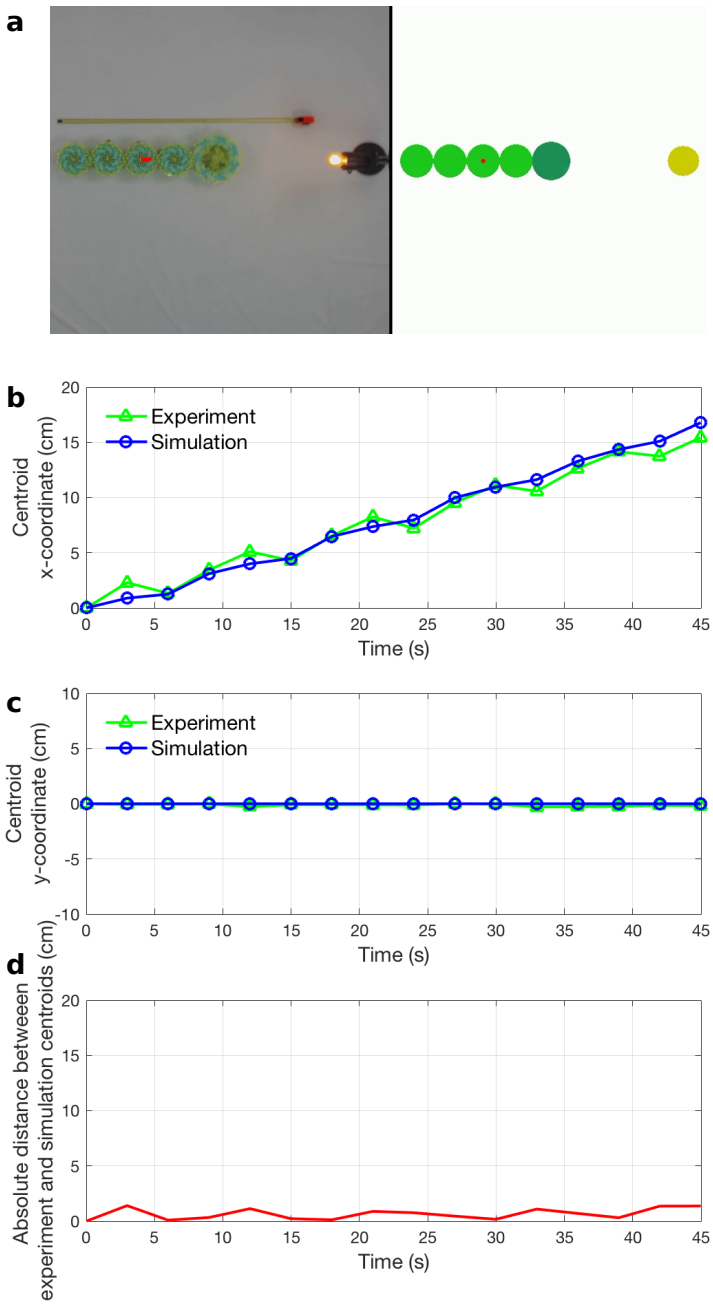

Figure S14. Simulation parameter fitting results, based on a five-particle linear robot. (a) Image of an experiment and the corresponding simulation model. (b) Plot comparing the x-coordinate of the centroids obtained experimentally and through simulation vs time. (c) Plot comparing the y-coordinate of the centroids obtained experimentally and through simulation vs time. (d) Plot of distance between the experimental and simulation-based centroids vs time (root mean square error is 0.8015 cm).

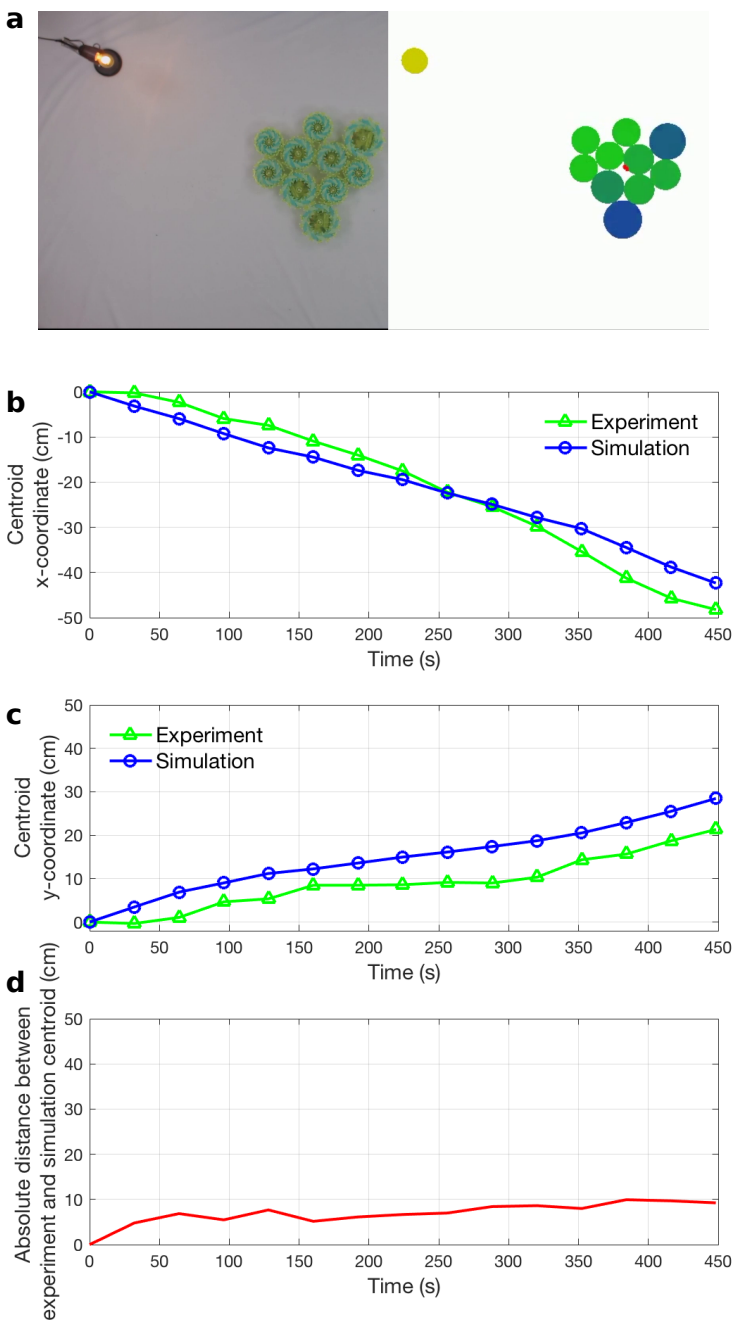

Figure S15: Simulation verification results based on a ten-particle amorphous robot. (a) Image of an experiment and the corresponding simulation model. (b) Plot comparing the x-coordinate of the centroids obtained experimentally and through simulation vs time. (c) Plot comparing the y-coordinate of the centroids obtained experimentally and through simulation vs time. (d) Plot of distance between the experimental and simulation-based centroids vs time (root mean square error is 7.3171 cm).

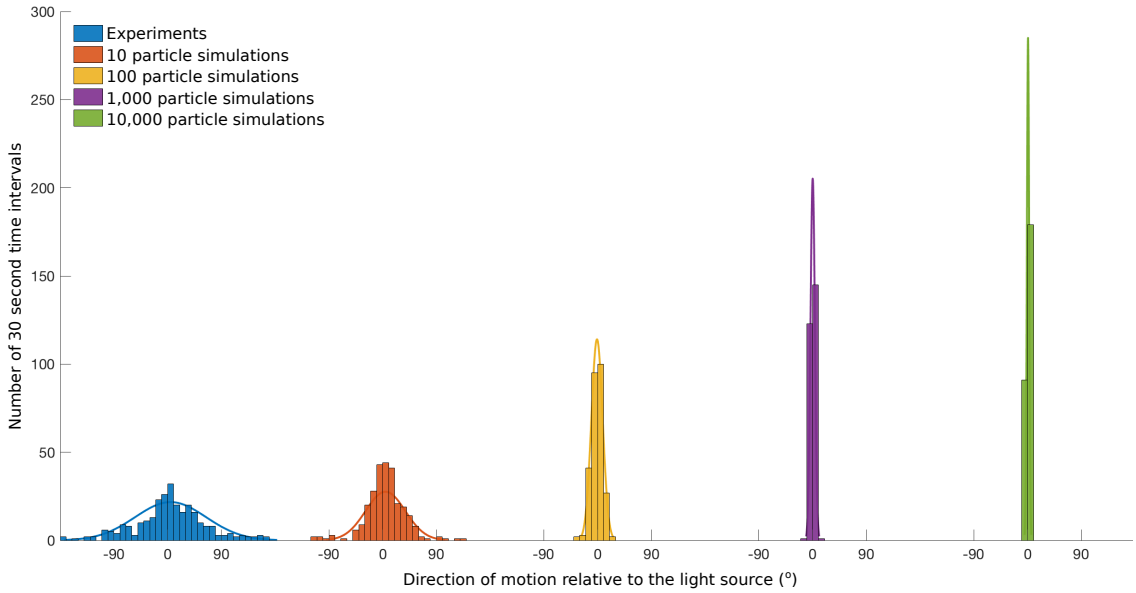

Figure S16: Variance of motion of particle robots. The angle of motion of the simulated particles towards the light source was measured every 30 seconds. Similar data from the physical experiments (Fig. 4d) is included here for comparison.

The simulation environment incorporated Compute Unified Device Architecture (CUDA) enabled GPUs for parallel processing to achieve tractable simulations at scale. Fig. S17 depicts the relationship between the execution time and particle robot size. The number of particle-to-particle interactions processed per (real-world) second is depicted on the same graph. It can be noted that, even though greater robot size corresponds to an increasing number of particle-particle interactions that need to be processed, the execution time remains approximately constant for robots comprising up to 10,000 particles. This finding indicates that resource utilization on the GPU employed (NVIDIA GTX 1070) is not saturated by the simulation environment when the robot consists of fewer than 10,000 particles. In fact, the increase in total number of interactions is balanced by the increase in number of particle-particle interactions processed per second by the simulation environment. Furthermore, using a single GPU is faster than real-time even when simulating a particle robot composed of 200,000 particles. While further increases in the robot size will cause a significant increase in the execution time, this may be mitigated by using multiple GPUs.

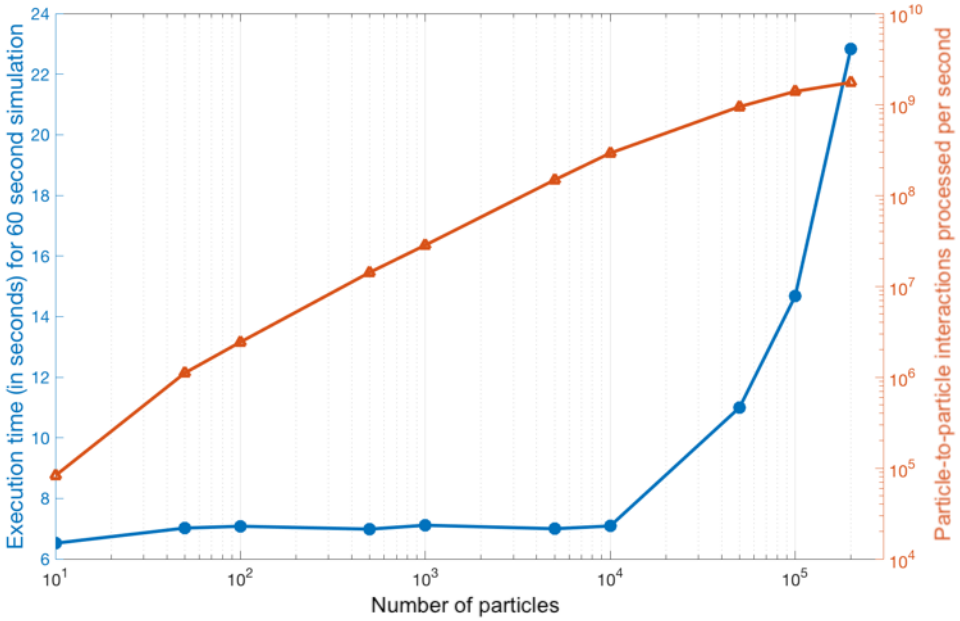

Figure S17: Simulation performance as measured by calculating particle-to-particle interactions per second.

S9. Simulation Studies and Results

The simulation environment was used to explore the effects of particle robots incorporating a certain percentage of dead (malfunctioning) particles at different scales. The percentage and number of dead particles was varied and simulated with eleven random configurations. The results are presented in Table S3, in mm/s, and Table S4, in percent of minimum diameter per cycle. As described above, the first 30 minutes of the simulation were not included in the speed calculation because the algorithm to place particles in random, amorphous configurations required a tradeoff between efficiency and particle density. During the first 30 minutes of the simulations, the particle configuration changes from sparse to dense, particularly when there are 10^3 particles or more.

Table S3. Speed of dead-particle simulations (mm/s)

No. of Particles	Percentage of Dead Particles								
	0%	10%	20%	30%	40%	50%	60%	70%	80%
10	1.24±0.44	0.95±0.50	0.74±0.47	0.37±0.50	0.21±0.26	0.17±0.30	0.01±0.07	-0.01±0.04	-0.00±0.00
100	0.64±0.19	0.43±0.09	0.31±0.11	0.16±0.07	0.84±0.04	0.03±0.02	0.00±0.00	0.00±0.00	0.00±0.00
1,000	0.45±0.05	0.33±0.04	0.22±0.02	0.13±0.02	0.63±0.01	0.02±0.01	0.01±0.01	0.00±0.00	0.00±0.00
10,000	0.27±0.01	0.20±0.01	0.14±0.01	0.09±0.01	0.05±0.00	0.02±0.00	0.01±0.00	0.00±0.00	0.01+0.00

Table S4. Speed of dead-particle simulations (% minimum diameter/cycle)

No. of Particles	Percentage of Dead Particles								
	0%	10%	20%	30%	40%	50%	60%	70%	80%
10	9.60±3.40	7.39±3.87	5.76±3.63	2.88±3.82	1.65±2.01	1.34±2.33	0.06±0.54	-0.07±0.32	-0.01±0.02
100	4.99±1.43	3.33±0.70	2.44±0.82	1.22±0.51	0.65±0.33	0.22±0.14	0.03±0.03	0.03±0.01	0.00±0.00
1,000	3.47±0.41	2.53±0.28	1.73±0.18	0.98±0.17	0.49±0.11	0.19±0.09	0.08±0.05	0.08±0.00	0.00±0.00
10,000	2.09±0.07	1.57±0.08	1.12±0.06	0.73±0.04	0.41±0.02	0.19±0.02	0.07±0.00	0.07±0.00	0.01+0.00

The simulation framework was also used to study the performance of particle robots when encountering an obstacle with a narrow gap. As in the dead-particle study, these simulations were defined using the physical particle characteristics and fitted coefficients. The number of particles were varied from 10, 100, 1000, and 10,000 particles. A parameter referred to as DPD (densest packing diameter) was defined to approximate the diameter of the particle robot, assuming all particles are contracted and in the most densely-packed circular configuration. The gap size was varied as a percentage of the DPD. This parameter was also used to define the distance of the

obstacle (0.75 DPD from the initial centroid) and the position of the light source (2.5 DPD from the initial centroid). These gap size amounts are listed in Tables S5 and S6 in centimeters and minimum particle diameter, respectively. The thickness of the obstacle was fixed to one minimum particle diameter. The particles that sense negligent light intensity (i.e. blocked by the obstacle) oscillate at the end of the cycle, as if defining the lowest end of the signal gradient.

Table S5. Gap sizes for varying number of particles with units in centimeters

Number of Particles	Densest Packing Diameter (cm)	20% Gap (cm)	30% Gap (cm)	40% Gap (cm)	50% Gap (cm)	60% Gap (cm)	70% Gap (cm)	80% Gap (cm)
10	59.1	11.82	17.73	23.64	29.55	35.46	41.37	47.28
50	123.2	24.64	36.96	49.28	61.60	73.92	86.24	98.56
100	171.8	34.36	51.54	68.72	85.90	103.08	120.26	137.44
500	374	74.80	112.20	149.60	187.00	224.40	261.80	299.20
1000	526.4	105.28	157.92	210.56	263.20	315.84	368.48	421.12
5000	1165.8	233.16	349.74	466.32	582.90	699.48	816.06	932.64
10000	1644.9	328.98	493.47	657.96	822.45	986.94	1151.43	1315.92

Table S6. Gap sizes for varying number of particles with units in particles (minimum diameter)

Number of Particles	Densest Packing Diameter (particles)	20% Gap (particles)	30% Gap (particles)	40% Gap (particles)	50% Gap (particles)	60% Gap (particles)	70% Gap (particles)	80% Gap (particles)
10	3.81	0.76	1.14	1.53	1.91	2.29	2.67	3.05
50	7.95	1.59	2.38	3.18	3.97	4.77	5.56	6.36
100	11.08	2.22	3.33	4.43	5.54	6.65	7.76	8.87
500	24.13	4.83	7.24	9.65	12.06	14.48	16.89	19.30
1000	33.96	6.79	10.19	13.58	16.98	20.38	23.77	27.17
5000	75.21	15.04	22.56	30.09	37.61	45.13	52.65	60.17
10000	106.12	21.22	31.84	42.45	53.06	63.67	74.29	84.90

While there are many different configurations and variables that could be tested, this study demonstrates the ability of particle robots to move through narrow gaps in obstacles. The results of the gap study are presented in Fig. S18 with the shaded area representing one standard deviation. By increasing the number of particles, there is greater success of particles passing through the gap and reduced variation of this behavior. Conversely, the results show the benefits of smaller, more numerous particles when adapting and maneuvering through narrow spaces. Again, the simulation environment is fit to the physical particles and not optimized for motion at large scales, and therefore the best performance is observed with 1,000 particles.

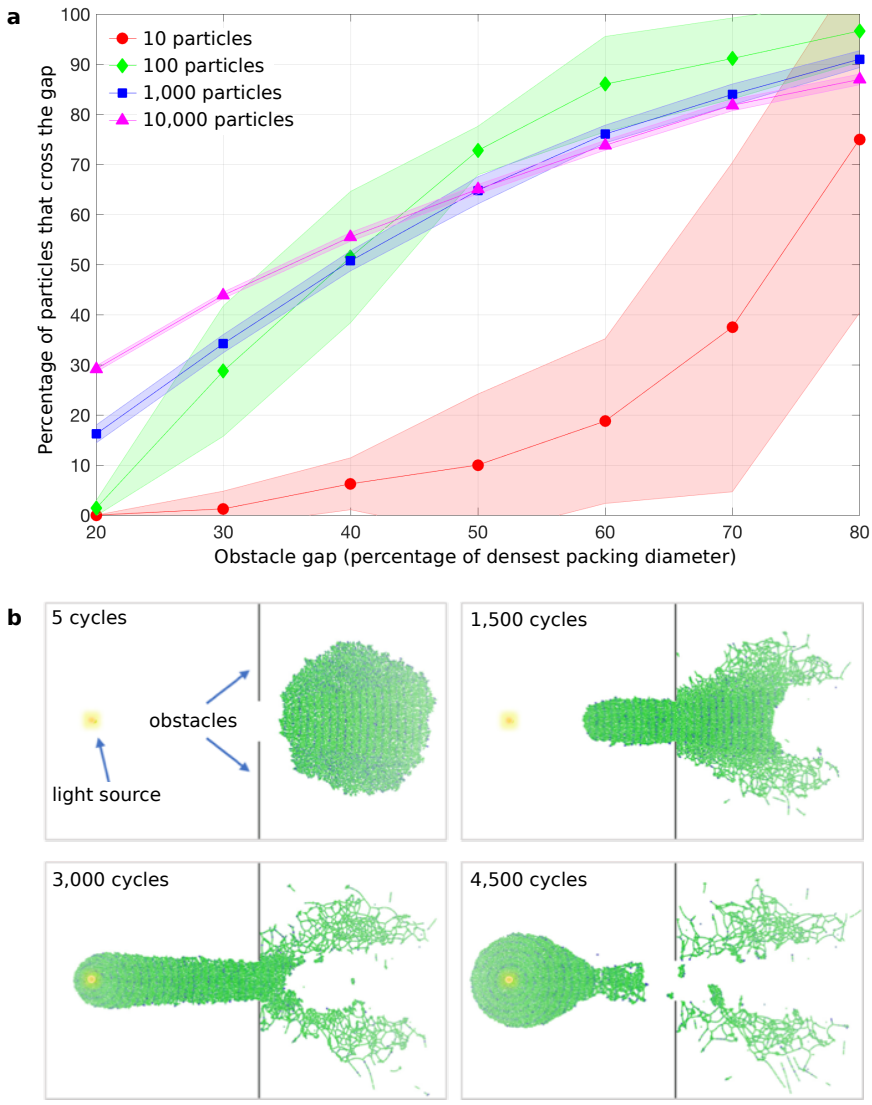

Figure S18: Particle motion through a narrow gap. (a) The number of particles are varied along with the gap size, which is proportional to the DPD. For each case, ten simulations were run for 4,500 cycles respectively. (b) An example of 10,000 particles moving through 30% DPD gap over time.

Furthermore, a study on carrying capacity was conducted to demonstrate the potential applications of particle robots with different numbers of particles. The object being transported is circular, with the same mass and friction coefficient as the particles. The parameter being tested was the size of the object, by varying the radius from 20%-80% DPD. Results are shown in Supplementary Video 6 and Fig. S19 for 1,000 particles. We found that 10 particles and 100 particles were unable to manipulate, and instead treated it as an obstacle. On the other hand, with

1,000 particles, the objects were carried a significant distance, however smaller objects were eventually left behind. 10,000 particles consistently carried the objects placed in front of their path, demonstrating the value of large-scale particle robots. While this study explored the effects of object size on carrying capacity, other variables can be studied, including mass of the object, friction between the object and surface, and attraction between the particles and the object.

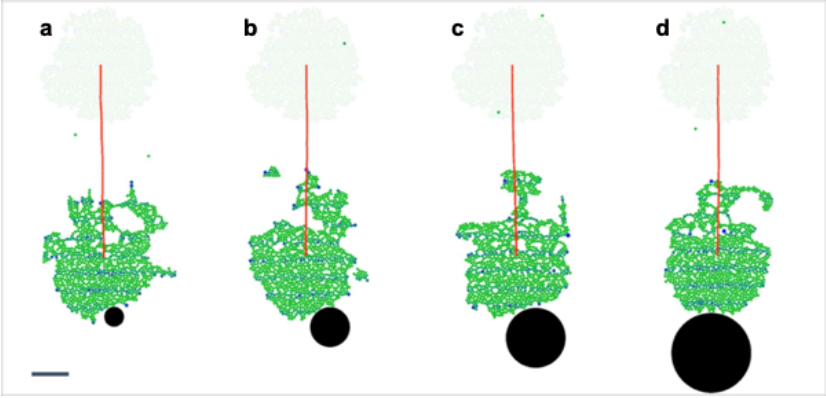

Figure S19. Carrying capacity of 1,000 particles. The circular object intended for transport, shown in black, has the mass and friction of a single particle and there is no attraction between the particles and the object. The diameter of the object was varied from (a) 20%, (b) 40%, (c) 60%, and (d) 80% of the densest packing diameter (DPD) of the particles**.** The motion is shown after approximately 3,000 expansion-contraction cycles. The scale bar represents 3 m.

A study of signal/sensor noise effect was conducted with 10,000-particle robots as well, given that they exhibited minimum variability with different random configurations. The stimulus signal (light) was detected by the sensor and used to interpret relative position of the particle and calculate its phase delay. In this test, the effect of varying the sensor noise for estimating incident light was explored. The noise power was characterized by the effect it has on distance estimation as a percentage of minimum particle diameter. For each level, particle robots were simulated in eleven random initial configurations. Fig. S20 shows the effects of sensor accuracy on the locomotion of these loosely-coupled robots. When the standard deviation of distance estimation error was equivalent to the minimum diameter of one particle, the system speed declined by 33%, and a standard deviation exceeding two particle diameters resulted in a stationary robot. The shaded area represents one standard deviation of the speed data.

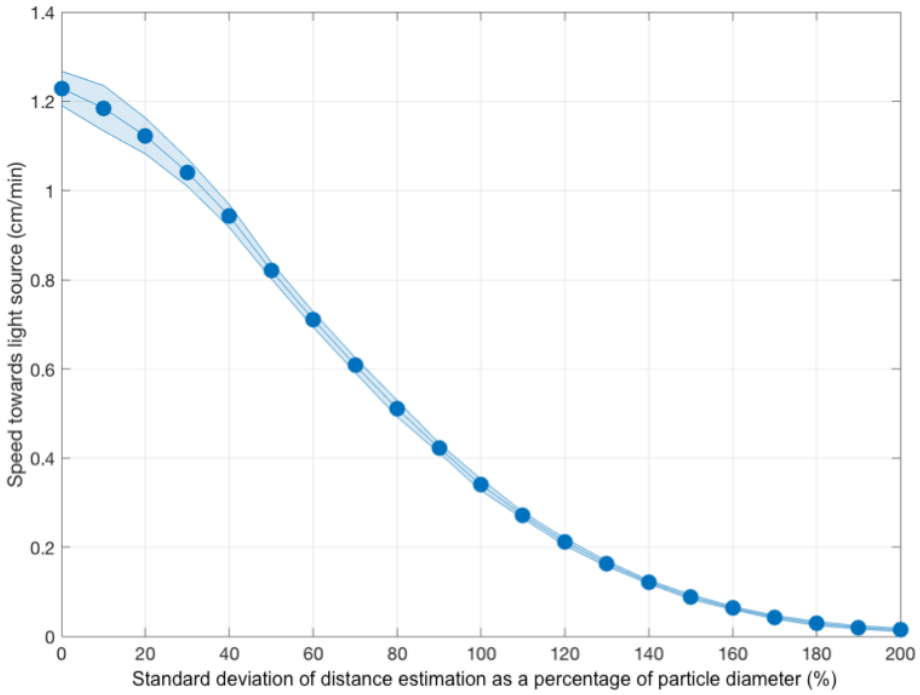

Figure S20: Effects of distance estimation error on average speed of 10,000-particle robots.

Lastly, Fig. S21 shows a simulation where "dead" particles are detached and new particles in the environment are annexed by the robot, increasing its size. It is evident that the overall speed and direction of the robot towards the light source does not change when doubling the number of particles.

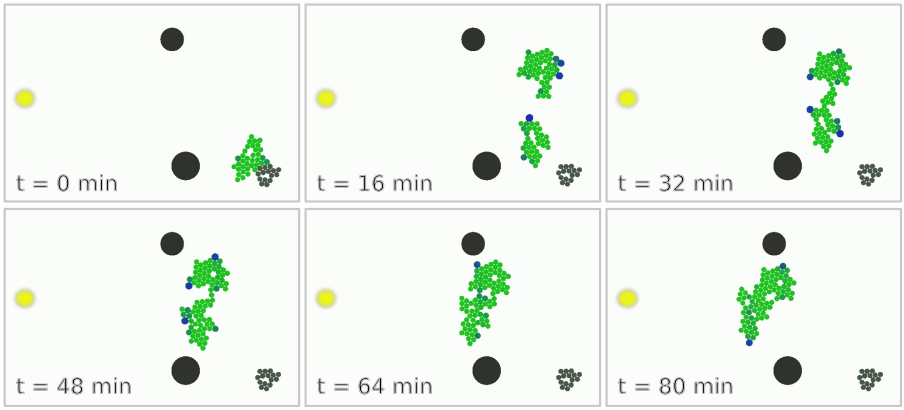

Figure S21: Demonstration of a particle robot capabilities. Particle robot detaches from "dead" particles and annexes additional particles from the environment while demonstrating phototaxis and obstacle avoidance.